

# DynoSurf: Neural Deformation-based Temporally Consistent Dynamic Surface Reconstruction

Yuxin Yao<sup>1</sup>, Siyu Ren<sup>1</sup>, Junhui Hou<sup>1\*</sup>, Zhi Deng<sup>2</sup>, Juyong Zhang<sup>3</sup>, Wenping Wang<sup>4</sup>

<sup>1</sup> City University of Hong Kong <sup>2</sup> Tencent Games

<sup>3</sup> University of Science and Technology of China <sup>4</sup> Texas A&M University

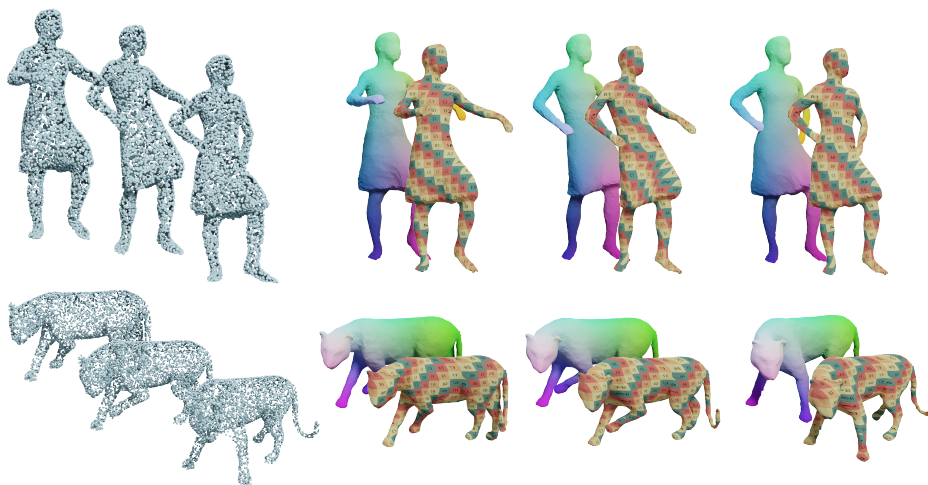


Figure 1: Temporally-consistent dynamic meshes (i.e., vertices are corresponded and connections are identical over time) reconstructed by our DynoSurf from time-varying 3D point cloud sequences (i.e., no temporal correspondence) **without** using any shape-prior, ground-truth surface, and ground-truth temporal correspondence. The color and texture map are used to illustrate correspondence across reconstructed mesh frames.

## Abstract

This paper explores the problem of reconstructing temporally consistent surfaces from a 3D point cloud sequence without correspondence. To address this challenging task, we propose DynoSurf, an unsupervised learning framework integrating a template surface representation with a learnable deformation field. Specifically, we design a coarse-to-fine strategy for learning the template surface based on the deformable tetrahedron representation. Furthermore, we propose a learnable deformation representation based on the learnable control points and blending weights, which can deform the template surface non-rigidly while maintaining the consistency of the local shape. Experimental results demonstrate the significant superiority of DynoSurf over current state-of-the-art approaches, showcasing its potential as a powerful tool for dynamic mesh reconstruction. The code is publicly available at <https://github.com/yaoyx689/DynoSurf>.

\*Corresponding author. Email: jh.hou@cityu.edu.hk. This work was supported by Hong Kong Research Grants Council under Grants 11202320 and 11219422.

# 1 Introduction

The reconstruction of temporally consistent geometric surfaces from a continuous dynamic 3D point cloud sequence without correspondences presents a valuable yet formidable challenge. These geometric surfaces play a crucial role in diverse domains, including film, gaming, animation, virtual reality (VR), augmented reality (AR), and robotics. They facilitate various applications such as motion object editing, texture transfer, and shape analysis, thereby contributing to the creation of realistic visual effects and immersive experiences.

With the development of the static surface reconstruction for a single object from a point cloud [17, 45, 38, 14], a natural idea to model the temporally consistent dynamic surfaces is to select a keyframe from the point cloud sequences and reconstruct it as a template surface through static reconstruction technology. Then the non-rigid deformation for the template surface is estimated by aligning it with other frames. High requirements are placed on the selection of the keyframe point cloud with fewer missing parts or occlusions and a similar shape to other frames. Some optimization-based dynamic reconstruction frameworks based on fusion continuously update the template shape during frame-by-frame non-rigid tracking [32, 9, 48]. These approaches are effective and pragmatic, but most of them use depth as input and cannot handle the sparse point clouds without any camera information. Some network-based method [34, 50, 21] no longer define or pre-establish the template shape, but jointly learn dynamic reconstruction. This way may achieve better results but increases the difficulty of decoupling the deformation field and the template space, which makes deformation have less practical significance. Moreover, these methods use ground truth to supervise training and have poor generalization. To address these problems, we first design an adaptive keyframe selection strategy and learn the template surface representation, then combine it with a deformation field to form a dynamic reconstruction framework. We reconstruct the temporally consistent surface by joint learning template surface and deformation field.

Furthermore, the design of the deformation field is particularly important. Optimization-based methods [23, 22, 55] often employ the embedded deformation graph [49] for non-rigid deformation, but they depend on the spatial position and mesh quality of the template surface. Some methods [60, 37, 51] directly use a network to predict the deformation for each point, lacking explicit control of the local structure. [5] proposes a neural deformation graph to reconstruct dynamic objects. However, they use this graph to reconstruct the geometric surface and non-rigid deformation simultaneously. This makes it need a more complex loss function, leading to the learning unstable. Therefore, we propose a deformation field based on explicit learnable control points, which improves the explicit controllability of the deformation field based on implicit representation. We also learn the blending weights between the points on the template surface and the control points. This allows us to adaptively learn the deformation consistency of surface points based on motion information.

In this paper, we aim to reconstruct a temporally consistent surface from continuous dynamic 3D point cloud sequences. We propose a reconstruction framework combining a template surface representation and a learnable deformation field based on the learnable control points and blending weight. Extensive experiments on three benchmark datasets demonstrate that our proposed temporally-consistent surface reconstruction outperforms the state-of-the-art methods to a large extent.

To summarize, our contributions are as follows:

- We propose a new learning framework for reconstructing temporally-consistent dynamic surfaces from time-varying point cloud sequences that can be trained *without* requiring any shape prior, ground-truth surface, and ground-truth temporal correspondence information as supervision.
- We propose a coarse-to-fine learning strategy for unsupervised static surface reconstruction based on the deformable tetrahedron representation.
- We propose a deformation representation based on learnable control points and blending weights that can better maintain local structure while being independent of object category.

# 2 Related Work

In this section, we briefly review the works closely related to our method, including 3D shape representation, non-rigid shape deformation, and sequential shape reconstruction.

**3D Shape Representation.** Generally, 3D shape representation could be divided into two main categories, explicit and implicit, and these can be transformed into one another. The point cloud and triangle mesh are the two most commonly utilized explicit representations for 3D shapes in various applications [40, 26, 58, 13, 12]. Implicit representation utilizes an isosurface of a field to depict a surface. The Binary Occupancy Field (BOF) [18, 31, 39, 4] and Signed Distance Field (SDF) [20, 27, 36] are two prevalent implicit fields for representing shapes, both dividing the entire space into two regions, inside and outside the shape. The implicit fields could be approximated by a neural network, such as DeepSDF [36], and SAL [1].

Given the shapes explicitly represented as point clouds or triangle meshes, diverse methods exist for their conversion into implicit representations [34, 18, 20, 27]. Conversely, when transforming implicit shapes into explicit forms, Marching Cubes (MC) [30] and Marching Tetrahedrons (MT) [33] stand out as the two widely used methods. Considering the detailed parts of shapes, DM Tet [45] and FlexiCubes [46] introduce offset for each tetrahedron or cube vertex, allowing their methodologies to effectively manage detailed shape components.

**Non-rigid Shape Deformation.** Deforming non-rigid shapes presents a challenge due to the high degree of freedom involved in controlling the shape deformation. To mitigate this, methods [23, 22] employ an embedded deformation graph [49] with local rigid properties for modeling deformation. During optimization, various geometric regularization terms, such as as-conformal-as-possible deformations [53] and as-rigid-as-possible deformations [54], are incorporated to impart meaningful deformation. Recently, QNS [55] and AMM [56] have developed the optimization methods to accelerate the optimization process.

With the advancement of deep learning in 3D vision, numerous learning-based deformation methods have been introduced. DispVoxNet [47] represents source and target shapes using voxel grids, learning an offset field supervised by ground truth offsets. In contrast, FlowNet3D [28] employs PointNet++ [41] to predict offsets for each point on the shapes. CorrNet3D [59] designs a symmetric pipeline to compute deformations between point clouds. RMA-Net [11] introduces a new deformation representation with a point-wise combination of several rigid transformations. NDP [24] proposes a non-rigid motion representation using a pyramid architecture.

**Sequential Shape Reconstruction.** Several 3D parametric models, such as SMPL [29] and SMAL [61], have been developed to represent general shapes within specific categories. These parametric models allow for straightforward adjustments in pose and shape by modifying their respective parameters. IPNet [8] integrates learned implicit fields with SMPL to control the poses of reconstructed human models. Following this, NPMs [35] disentangle shapes and poses into latent spaces, enhancing reconstruction accuracy. Conversely, H4D [16] and LoRD [15] initially regress SMPL model parameters to align with each frame of given point clouds. Subsequently, vertex-wise offsets are applied to the resulting SMPL models, approximating the reconstructed shapes to match the provided point cloud sequence. However, these methods are constrained to handling sequences within specific categories, limiting their broad applicability.

Recent studies [32, 34, 50, 5] have expanded the scope of reconstructing dynamic shapes by predicting deformation fields between different frames. Approaches like Dynamic Fusion [32] and NDG [5] establish a deformation graph to capture the deformation fields. O-Flow [34] extends ONet [31] from 3D to 4D, representing deformation fields with a Neural-ODE [6], while LPDC [50] employs MLPs to model correspondences in parallel. Both O-Flow and LPDC reconstruct the reference shape based on the initial frame, with subsequent frames having their query points mapped to the chosen reference frame. In contrast, I3DMM [57] learns a canonical reference shape for sequences of heads, while CASPR [43] and Garment Nets [7] use ground truth canonical coordinates for network training, which is often impractical. Cadex [21] employs canonical map factorization to represent deformation without requiring correspondences during training, but it may struggle with sequences featuring substantial motions.

## 3 Proposed Method

### 3.1 Problem Statement and Method Overview

Let  $\mathcal{P} = \{\mathbf{P}_1, \dots, \mathbf{P}_K\}$  be a *time-varying* 3D point cloud sequence capturing the geometric changes or motion of scenes/objects over time, where the correspondence across frames is unknown and

$\mathbf{P}_k \in \mathbb{R}^{N_k \times 3}$  is the  $k$ -th ( $k \in [1, K]$ ) frame containing  $N_k$  points. We aim to reconstruct from  $\mathcal{P}$  a *temporally-consistent* mesh sequence  $\mathcal{M} = \{\mathbb{M}_1, \dots, \mathbb{M}_K\}$ , where the  $k$ -th mesh surface  $\mathbb{M}_k := \{\mathbf{V}_k, \mathcal{E}\}$  with  $\mathbf{V}_k$  and  $\mathcal{E}$  being the vertex set and connection set, respectively, the vertices across meshes are corresponded, and all meshes share the same  $\mathcal{E}$ .

To address this challenging task, we propose an *unsupervised* learning framework, named DynoSurf, which requires no ground-truth surface and correspondence information as supervision. As illustrated in Fig. 2, DynoSurf mainly consists of two stages: template surface construction (Sec. 3.2) and deformation-based temporal reconstruction (Sec. 3.3). Generally, we first select a keyframe from  $\mathcal{P}$  and reconstruct its surface based on the deformable tetrahedron representation through a coarse-to-fine learning process. Then, we deform the enhanced template surface to simultaneously align with all frames of  $\mathcal{P}$  by learning a control points blending-based deformation field through jointly optimizing the template surface and deformation field. In what follows, we will detail the framework.

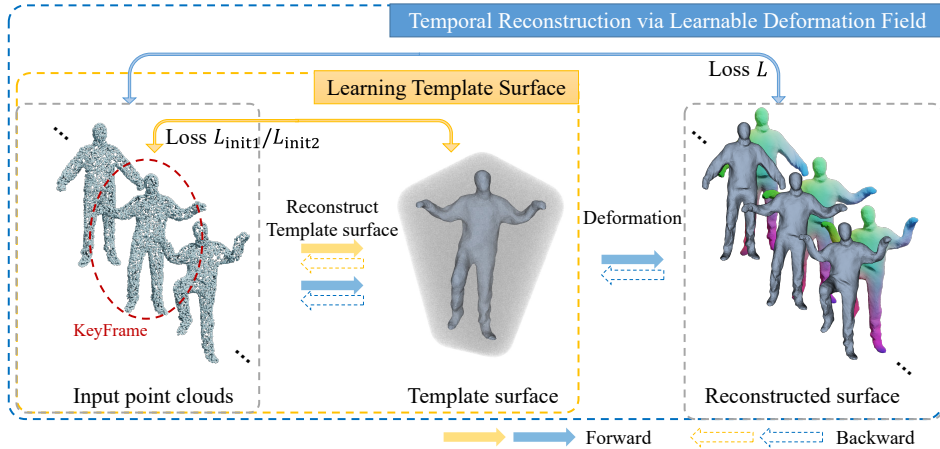


Figure 2: Illustration of the proposed DynoSurf, which can reconstruct from time-varying point cloud sequences temporally-consistent dynamic surfaces without requiring any ground-truth surface and temporal correspondence information.

### 3.2 Template Surface Representation via Deformable Tetrahedron

In this stage, we aim to construct a template surface, i.e., a mesh fitting the selected point cloud from  $\mathcal{P}$ , called keyframe. As illustrated in Fig. 3, we initially select a keyframe, denoted as  $\mathbf{P}_{k^*} \in \mathcal{P}$ , and construct its convex hull as a triangle mesh, referred to as  $\mathbb{C}$ . Subsequently, we process  $\mathbb{C}$  to generate a tetrahedron mesh, denoted as  $\mathbb{T}$ , where the signed distance field (SDF) of the surface underlying  $\mathbf{P}_{k^*}$  is defined and learned through a coarse-to-fine learning process. The SDF enables us to extract a mesh, denoted as  $\overline{\mathbb{M}} := \{\overline{\mathbf{V}}, \mathcal{E}\}$  with  $\overline{\mathbf{V}}$  being the vertex set.

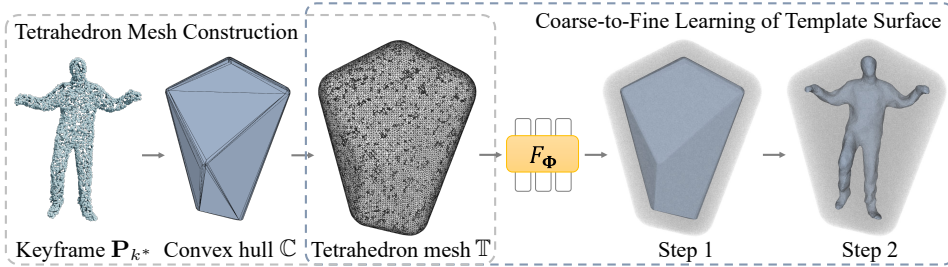


Figure 3: Illustration of the pipeline of learning template surface via deformable tetrahedron.

**Keyframe selection and tetrahedron mesh construction.** Since we will deform the reconstructed template surface from  $\mathbf{P}_{k^*}$  for temporal reconstruction in the following deformation stage, intu-

itively,  $\mathbf{P}_{k^*}$  should be relatively average to facilitate the deformation process. Thus, we determine  $k^* = \arg \min_{k \in [1, K]} \sum_l \text{CD}_{\ell_2}(\mathbf{P}_k, \mathbf{P}_l)$ , where  $\text{CD}_{\ell_2}(\cdot, \cdot)$  computes the  $\ell_2$ -norm-based Chamfer distance between two point clouds. We then adopt QuickHull [2] to construct the convex hull  $\mathbb{C}$  of  $\mathbf{P}_{k^*}$ , which is further dilated and re-meshed to obtain a uniform triangle mesh  $\widehat{\mathbb{C}}$  surrounding  $\mathbb{C}$ . By tetrahedralizing  $\widehat{\mathbb{C}}$ , we obtain a tetrahedron mesh  $\mathbb{T} = \{\mathbf{Q}, \mathbf{T}\}$  with  $\mathbf{Q} = \{\mathbf{q}_1, \dots, \mathbf{q}_{|\mathbf{Q}|}\}$  and  $\mathbf{T} = \{\mathbf{T}_1, \dots, \mathbf{T}_{|\mathbf{T}|}\}$  being the vertex and tetrahedron sets, respectively. Note that the vertices of  $\mathbb{T}$  are distributed both inside and outside of  $\mathbb{C}$  due to the dilation and remeshing operations.

**Coarse-to-fine learning of deformable tetrahedron-based template surface.** We learn the deformation tetrahedron representation [45] to construct a template surface  $\overline{\mathbb{M}}$  that approximates the point surface  $\mathbf{P}_{k^*}$ . Specifically, for each vertex  $\mathbf{q} \in \mathbf{Q}$ , we train an MLP  $F_{\Phi}(\cdot)$  parameterized with  $\Phi$  to learn the SDF value  $s(\mathbf{q})$  and the displacement vector  $\delta(\mathbf{q})$  with respect to the surface  $\overline{\mathbb{M}}$ :

$$[s(\mathbf{q}), \delta(\mathbf{q})] = F_{\Phi}(\Gamma(\mathbf{q})), \quad (1)$$

where  $\Gamma(\cdot)$  is the Position Encoding operator. Then, based on the deformed tetrahedral grid points  $\{\mathbf{q} + \delta(\mathbf{q})\}_{\mathbf{q} \in \mathbf{Q}}$  and  $\{s(\mathbf{q})\}_{\mathbf{q} \in \mathbf{Q}}$ , we can employ the differentiable marching tetrahedron algorithm [45], denoted as  $\text{DMT}(\cdot, \cdot)$ , to extract  $\overline{\mathbb{M}}$ , i.e.,  $\overline{\mathbb{M}} = \text{DMT}(\{\mathbf{q} + \delta(\mathbf{q})\}, \{s(\mathbf{q})\})$ .

To train  $F_{\Phi}(\cdot)$  to encode the SDF of the surface  $\overline{\mathbb{M}}$ , we adopt the following coarse-to-fine strategy to make the learning process easier and faster: (1) We initialize  $F_{\Phi}(\cdot)$  by learning the SDF of  $\mathbb{C}$ , i.e.,

$$\min_{\Phi} L_{\text{init1}} = \sum_{\mathbf{q} \in \mathbf{Q}} \|s(\mathbf{q}) - \text{SDF}(\mathbf{q}, \mathbb{C})\|^2, \quad (2)$$

where  $s(\mathbf{q})$  is the predicted SDF value of  $F_{\Phi}(\cdot)$  and  $\text{SDF}(\mathbf{q}, \mathbb{C})$  denotes the ground-truth SDF value of convex hull surface  $\mathbb{C}$  at  $\mathbf{q}$ . (2) We then refine  $F_{\Phi}(\cdot)$  by constraining  $\overline{\mathbb{M}}$  and  $\mathbf{P}_{k^*}$  to be as close as possible, i.e.,

$$\min_{\Phi} L_{\text{init2}} = \tilde{w}_1 L_{\text{CD}} + \tilde{w}_2 L_{\text{Norm}}^* + \tilde{w}_3 L_{\text{SDF}}, \quad (3)$$

where  $L_{\text{CD}} := \text{CD}_{\ell_1}(\overline{\mathbb{M}}, \mathbf{P}_{k^*})$  denotes the  $\ell_1$ -norm-based Chamfer distance between  $\overline{\mathbb{M}}$  and  $\mathbf{P}_{k^*}$ ;  $L_{\text{Norm}}^* := \text{NC}_{\ell_1}(\overline{\mathbb{M}}, \mathbf{P}_{k^*})$  measures the consistency of the corresponding normals (see the *Supplementary Material* for the definition of  $L_{\text{Norm}}^*$ );  $L_{\text{SDF}}$  is employed to promote the accuracy of the learned SDF, defined as

$$L_{\text{SDF}} = \frac{1}{|\mathbf{Q}|} \sum_{\mathbf{q} \in \mathbf{Q}} |s(\mathbf{q}) - \text{SDF}_{\text{IMLS}}(\mathbf{q}, \mathbf{P}_{k^*})|, \quad (4)$$

where  $\text{SDF}_{\text{IMLS}}(\mathbf{q}, \mathbf{P}_{k^*})$  is the SDF value at  $\mathbf{q}$  approximated through implicit moving least-squares [20]:

$$\text{SDF}_{\text{IMLS}}(\mathbf{q}, \mathbf{P}_{k^*}) = \frac{\sum_{\mathbf{p}_j \in \mathcal{N}(\mathbf{q})} \theta(\|\mathbf{q} - \mathbf{p}_j\|, \zeta) \cdot \langle \mathbf{q} - \mathbf{p}_j, \mathbf{n}_j \rangle}{\sum_{\mathbf{p}_j \in \mathcal{N}(\mathbf{q})} \theta(\|\mathbf{q} - \mathbf{p}_j\|, \zeta)}, \quad (5)$$

where  $\mathcal{N}(\mathbf{q})$  denotes the set of nearest points in  $\mathbf{P}_{k^*}$ .  $\theta(d, \zeta) = \exp(-d^2/\zeta^2)$  is the weight function. We set  $|\mathcal{N}(\mathbf{q})| = 10$  and  $\zeta = 0.1$  by default.

**Remark.** It is worth noting that the resulting template surface  $\overline{\mathbb{M}}$  will be *adaptively* updated/enhanced during the following deformation stage to facilitate the deformation stage, thus promoting the quality of reconstructed surfaces of the remaining point cloud frames of  $\mathcal{P}$ .

### 3.3 Temporal Reconstruction via Learnable Deformation Field

In this stage, as illustrated in Fig. 4, we propose a learnable deformation field based on control points blending. This deformation field enables us to deform the *adaptively-enhanced* template surface to achieve temporal reconstruction. By employing this approach, we ensure the temporal consistency of the reconstructed surface sequence.

**Control points blending-based learnable deformation field.** We first build a set of control point  $\mathbf{U} := \{\mathbf{u}_1, \dots, \mathbf{u}_{|\mathbf{U}|}\}$ , which are obtained using the farthest point sampling (FPS) algorithm [10] on the vertex set of the tetrahedron mesh  $\mathbb{T}$  (i.e.,  $\mathbf{Q}$ ) such that the control points  $\mathbf{u}_r$ ,  $r = 1, 2, \dots, |\mathbf{U}|$  are uniformly distributed in  $\mathbb{T}$ . Note that the positions of initial control points are also adaptively

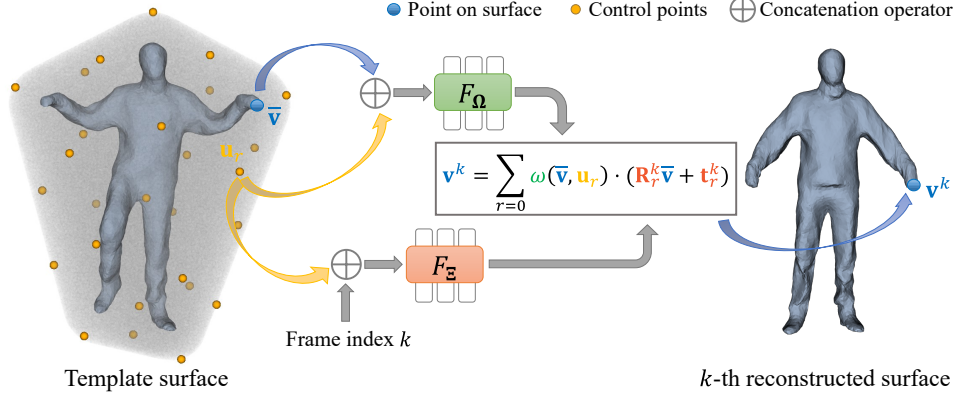


Figure 4: Illustration of the proposed control points blending-based learnable deformation stage for temporal reconstruction. Note that the adaptively enhanced template surface will be deformed to all frames.

optimized during training to make the deformation more flexible. We associate each  $\mathbf{u}_r$  with a rotation matrix  $\mathbf{R}_r^k \in \text{SO}(3)$  and a translation  $\mathbf{t}_r^k \in \mathbb{R}^3$  for each frame  $\mathbf{P}_k$ ,  $k = 1, 2, \dots, K$ . Then for each vertex of the template surface  $\bar{\mathbf{v}} \in \bar{\mathbf{V}}$ , which is the vertex set of the surface  $\bar{\mathbb{M}}$ , the deformed vertex at the  $k$ -th frame is represented as

$$\mathbf{v}^k = \sum_{r=1}^{|\mathbf{U}|} \omega(\bar{\mathbf{v}}, \mathbf{u}_r) \cdot (\mathbf{R}_r^k \bar{\mathbf{v}} + \mathbf{t}_r^k), \quad (6)$$

with the weight  $\omega(\bar{\mathbf{v}}, \mathbf{u}_r)$  learned via

$$\omega(\bar{\mathbf{v}}, \mathbf{u}_r) = \frac{\exp(F_\Omega([\bar{\mathbf{v}} \| (\bar{\mathbf{v}} - \mathbf{u}_r)]))}{\sum_{r=1}^{|\mathbf{U}|} \exp(F_\Omega([\bar{\mathbf{v}} \| (\bar{\mathbf{v}} - \mathbf{u}_r)]))}, \quad (7)$$

where  $F_\Omega(\cdot)$  is an MLP parameterized with  $\Omega$ , and  $[\cdot \| \cdot]$  is the concatenation operator. We initialize  $\omega(\bar{\mathbf{v}}, \mathbf{u}_r)$  as

$$\tilde{\omega}(\bar{\mathbf{v}}, \mathbf{u}_r) = \frac{\exp(-\|\bar{\mathbf{v}} - \mathbf{u}_r\|^2 / 2\eta^2)}{\sum_{r=1}^{|\mathbf{U}|} \exp(-\|\bar{\mathbf{v}} - \mathbf{u}_r\|^2 / 2\eta^2)}, \quad (8)$$

where  $\eta = 0.1$  by default. The reconstructed surface of  $\mathbf{P}_k$  can be obtained as  $\mathbb{M}_k = \{\mathbf{V}_k, \mathcal{E}\}$  with  $\mathbf{V}_k$  being the collection of  $\mathbf{v}^k$ .

We also utilize an MLP  $F_\Xi(\cdot)$  parameterized with  $\Xi$  to learn the deformation transformations of all frames, i.e.,

$$[\xi_r^k, \mathbf{t}_r^k] = F_\Xi(\Gamma([\mathbf{u}_r \| k])), \quad (9)$$

where  $\xi_r^k \in \text{so}(3)$  is the Lie algebra format of  $\mathbf{R}_r^k$ . Owing to the spectral bias property of neural networks [42], the learned transformations would vary smoothly in both spatial and temporal domains to ensure the spatial and temporal smoothness of the constructed mesh sequence.

**Remark.** It's worth noting that our deformation formula is different from the neural deformation graph in [5], which only defines the importance weight for each graph node, and blends them according to the spatial positions. Here, we use an MLP to parameterize the weights of any point in space. Additionally, it confines the node positions within the object. These constraints limit the flexibility of the deformation. The surface deformation in RMA-Net [11] is defined based on globally shared transformations, which limits the ability to capture the locally correlated characteristics of non-rigid object deformations. By using control points-blending, we can effectively enhance the representation capability of the deformation.

**Learning of deformable field with enhanced template surface.** Instead of solely focusing on training the deformation stage, i.e.,  $F_\Omega(\cdot)$ ,  $F_\Xi(\cdot)$  and  $\mathbf{U}$ , we jointly train the deformation stage and the template surface representation, i.e.,  $F_\Phi(\cdot)$  has been warmed-up in the first stage. Specifically, at each iteration, we extract the template surface using  $\text{DMT}(\cdot, \cdot)$  and then deform it to all frames

for temporally consistent reconstruction. Through joint optimization, we aim to enhance the adaptability of the template surface to the deformation process, ultimately leading to improved temporal reconstruction quality. To achieve this goal, we consider the following loss function:

$$\min_{\Phi, \Omega, \Xi, \mathbf{U}} L = w_1 L_{\text{R-CD}} + w_2 L_{\text{Norm}} + w_3 L_{\text{R-SDF}} + w_4 L_{\text{Smo}} + w_5 L_{\text{Shape}}. \quad (10)$$

Specifically,  $L_{\text{R-CD}}$  stands for the proposed robust Chamfer distance to cope with point clouds with holes and outliers, defined as  $L_{\text{R-CD}} = \frac{1}{K} \sum_k L_{\text{R-CD}}^k$  with

$$L_{\text{R-CD}}^k = \frac{1}{|\tilde{\mathbf{V}}_k|} \sum_{\mathbf{v}_i \in \tilde{\mathbf{V}}_k} \phi_\alpha(\mathbf{v}_i, \mathbf{p}_{\rho_i}) \cdot \|\mathbf{v}_i - \mathbf{p}_{\rho_i}\|^2 + \frac{1}{|\mathbf{P}_k|} \sum_{\mathbf{p}_j \in \mathbf{P}_k} \phi_\alpha(\mathbf{p}_j, \mathbf{v}_{\tau_j}) \cdot \|\mathbf{p}_j - \mathbf{v}_{\tau_j}\|^2, \quad (11)$$

where  $\tilde{\mathbf{V}}_k$  is the set of points uniformly sampled from  $\mathbb{M}_k$  with the size of  $10^4$  by default, and  $\phi_\alpha(x, y) = \exp(-\alpha \cdot \|x - y\|^2)$ . The normal loss term  $L_{\text{Norm}} = \sum_k \text{NC}_{\ell_1}(\tilde{\mathbf{V}}_k, \mathbf{P}_k)/K$  constrains the consistency of normals.

The proposed robust SDF loss term  $L_{\text{R-SDF}}$  regularizes the orientation of the deformed mesh, defined as

$$L_{\text{R-SDF}} = \frac{1}{K \cdot |\mathbf{Q}_s|} \sum_{\mathbf{q} \in \mathbf{Q}_s} \sum_k \bar{\psi}_\beta^k(\mathbf{q}) \cdot |f_\gamma(s(\hat{\mathbf{q}}^k)) - f_\gamma(\text{SDF}_{\text{IMLS}}(\hat{\mathbf{q}}^k, \mathbf{P}_k))|, \quad (12)$$

where  $\hat{\mathbf{q}}^k$  is the deformed positions of  $\mathbf{q}$  according to Eq. (6);  $\bar{\psi}_\beta^k(\mathbf{q}) = \frac{\psi_\beta^k(\mathbf{q})}{\sum_k \psi_\beta^k(\mathbf{q})}$  with  $\psi_\beta^k(\mathbf{q}) = \exp(-\beta \cdot |\text{SDF}_{\text{IMLS}}(\hat{\mathbf{q}}^k, \mathbf{P}_k)|^2)$  and  $\beta = 50$  is to measure the confidence of each term. That is, when the deformed point  $\hat{\mathbf{q}}^k$  has a smaller value in the SDF approximated by the target point cloud, it is closer to the surface, and we assume that it is more accurate;  $\mathbf{Q}_s$  is a subset of size  $|\mathbf{Q}_s| = 10^4$  randomly sampled from  $\mathbf{Q}$ .  $f_\gamma(x) = \frac{1}{1 + \exp(-\gamma \cdot x)}$  with  $\gamma = 10^2$  is used to scale the amplified SDF value to  $(0, 1)$  because we pay more attention to whether the point  $\hat{\mathbf{q}}^k$  is inside or outside the surface.

The loss term  $L_{\text{Smo}}$  ensures the smoothness of the deformation, defined as

$$L_{\text{Smo}} = \frac{1}{2K|\mathcal{E}|} \sum_k \sum_{l \in \mathcal{I}(k)} \sum_{(\mathbf{v}_i, \mathbf{v}_j) \in \mathcal{E}} \|(\mathbf{v}_i^k - \mathbf{v}_i^l) - (\mathbf{v}_j^k - \mathbf{v}_j^l)\|^2, \quad (13)$$

where  $\mathcal{I}(k) = \{k-1, k+1\}$ . When  $k=1$  or  $k=K$ , we only use one neighbor point cloud frame. Finally, it is crucial to ensure that the enhanced template surface maintains a reasonable shape throughout the joint optimization process. Thus, we constrain the deformation field of the template surface as unit transformation as possible with a loss term  $L_{\text{Shape}}$ :

$$L_{\text{Shape}} = \sum_{\mathbf{u}_r \in \mathbf{U}} \|[\xi_r^{k*}, \mathbf{t}_r^{k*}]\|^2, \quad (14)$$

where  $[\xi_r^{k*}, \mathbf{t}_r^{k*}] \in \mathbb{R}^6$  denotes the rotation matrix represented by Lie algebra format and translation vector of the keyframe.

## 4 Experiments

### 4.1 Experimental Settings

**Implementation details.** In our approach, we employed Multi-Layer Perceptrons (MLPs) consisting of 5 linear layers with a feature dimension of 128 to implement  $F_\Phi(\cdot)$ ,  $F_\Xi(\cdot)$ , and  $F_\Omega(\cdot)$ . The default weights setting in the loss function are listed in Tab. 1. Training was conducted using the ADAM optimizer [19] with a learning rate of  $1 \times 10^{-4}$ . We performed all experiments on a single NVIDIA A6000 GPU.

**Datasets.** We utilized three well-established benchmark datasets, namely DFA-UST [3], DT4D [25], and AMA [52], for our evaluation. From motion sequences, we selected 17 consecutive frames to form a set of input point clouds. Randomly sampling 5000 points from the ground truth mesh, we ensured diversity in our point cloud selection. Adopting the train and test data splits provided by [21], we used 109 sets and 89 sets from the test data of the DFAUST dataset and DT4D-animal dataset, respectively. The AMA dataset comprises 10 motion sequences; for supervised

Table 1: Default parameter settings and runtime. For the learning template surface, we listed iterations and running time for coarse/fine stage.

Learning template surface					Temporal reconstruction						
$\tilde{w}_1$	$\tilde{w}_2$	$\tilde{w}_3$	#Iters	Time	$w_1$	$w_2$	$w_3$	$w_4$	$w_5$	#Iters	Time
500	0.001	50	$10^3/5000$	10 s/2 mins	500	0.001	100	$10^3$	1	$10^4$	30 mins

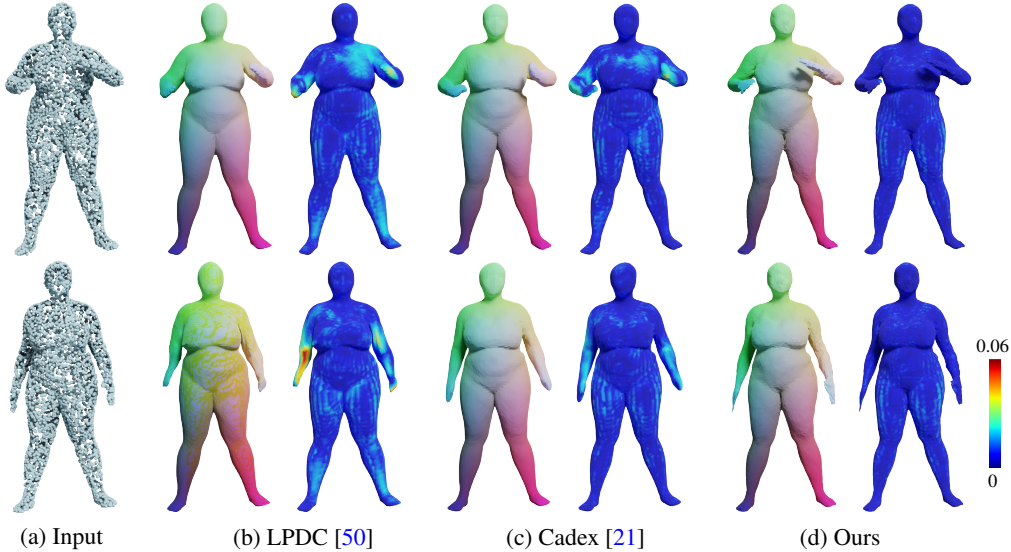


Figure 5: Comparison of visual results by different methods on the DFAUST dataset.

learning comparison methods, we employed 1176 sets from 7 sequences as the train set and 32 sets of point clouds from the remaining 3 sequences (“crane”, “march1” and “samba”) as the test set. To maintain consistency across sequences, we normalized the diagonal length of the bounding box in the first frame to 1 and centered it at the origin of the coordinates. Subsequent point clouds underwent transformations based on the scale and translation of the first frame. We utilized Meshlab’s point cloud estimation normal method for normal estimation and adjusted the normal directions to face outward.

Table 2: Quantitative comparisons of different methods on three datasets.

Dataset	Method	CD ( $\times 10^{-4}$ ) ↓	NC ↑	F-0.5% ↑	F-1% ↑	Corr. ( $\times 10^{-2}$ ) ↓
DFAUST [3]	LPDC [50]	2.430	0.929	0.299	0.633	1.46
	Cadex [21]	1.062	0.941	0.519	0.823	1.28
	Ours	0.688	0.953	0.894	0.985	1.02
DT4D [25]	Cadex [21]	22.377	0.868	0.269	0.532	4.99
	Ours	1.036	0.933	0.582	0.870	3.23
AMA [52]	LPDC [50]	108.822	0.666	0.045	0.101	14.1
	Cadex [21]	71.041	0.663	0.052	0.119	13.6
	Ours	0.320	0.918	0.943	0.683	4.44

**Methods under comparison.** We conducted a comparative analysis involving our proposed method and two cutting-edge techniques specialized in dynamic surface reconstruction from sequences of point clouds: LPDC [50] and Cadex [21]. *Note* that both Cadex and LPDC necessitate *ground-truth occupancy values* and *ground-truth correspondences* for supervision during training. For Cadex, we employed the officially released pre-trained model provided by the authors for testing on DFAUST and DT4D datasets. As for LPDC, the authors exclusively performed experiments on the DFAUST dataset and released the pre-trained model. To ensure a comprehensive comparison, we introduced the AMA dataset, a human body dataset characterized by *significantly larger* defor-



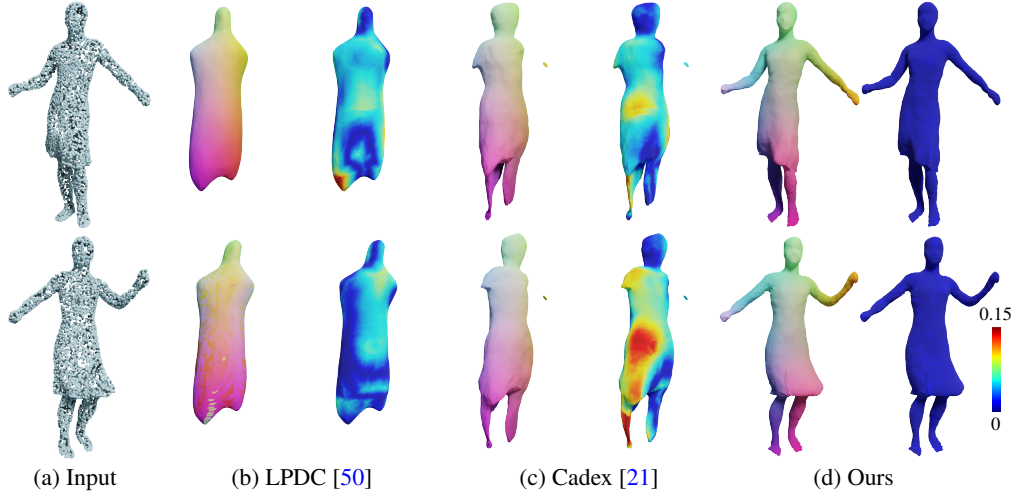


Figure 6: Comparison of visual results by different methods on the AMA dataset

mation and movement ranges compared to DFAUST. Furthermore, we retrained Cadex and LPDC on the AMA dataset.

**Evaluation metrics.** Following previous works [31, 21, 38], we scaled the test data to its original size and quantitatively assessed various methods using  $\ell_2$ -norm-based Chamfer Distance (CD), Normal Consistency (NC), F-score with thresholds of 0.5% (F-0.5%) and 1% (F-1%), and Correspondences Error (Corr.) to evaluate different methods quantitatively. For the visual results, we assigned the same colors to corresponded vertices to indicate the accuracy of learned correspondences by different methods. In addition, we also visualized the pointwise distance error from the ground-truth surface.

## 4.2 Comparisons with State-of-the-Art Methods

**Results of clean and complete data.** Table 2 shows the comparison of our method against state-of-the-art methods on the three datasets. The results demonstrate that our method attains the highest accuracy. The visual comparisons in Figs. 5 and 6 further validate the significant superiority of our method. Notably, Cadex and LPDC exhibit notably poor performance on the AMA dataset. This discrepancy could be attributed to the smaller data volume of the AMA dataset compared to DFAUST and DT4D, shedding light on the limitations of these supervised learning methods. We also refer readers to the *Supplementary Material* and *Video Demo* for more visual results.

**Results of noisy and partially missing data.** We also evaluate the performance of our method on noisy data. We add 0.5% Gaussian noise for each point in a point cloud sequence in DFAUST dataset [3] and show the results in Fig. 7. Since point cloud data collected by real-depth cameras often contain missing parts, we tested the situation when there are some holes in the surface. For a sequence in "swing" motion sequences of AMA dataset [52], we placed two virtual cameras in front of and behind the mesh model for simulated acquisition and merged the point clouds scanned by the two cameras. Fig. 7 shows the performance of our method and the variants. We can see that our method can reconstruct partially missing meshes. More results are presented in the *Supplementary Material*.

## 4.3 Ablation Study

In this section, we conducted thorough ablation studies targeting key components of our framework on the AMA dataset, where we took 1 set from each sequence and 10 sets in total for data diversity. We focused on the following aspects:

**1) Learnable deformation field.** To evaluate the effectiveness of the proposed deformation field, we conducted experiments by maintaining the other components and substituting the deformation field:

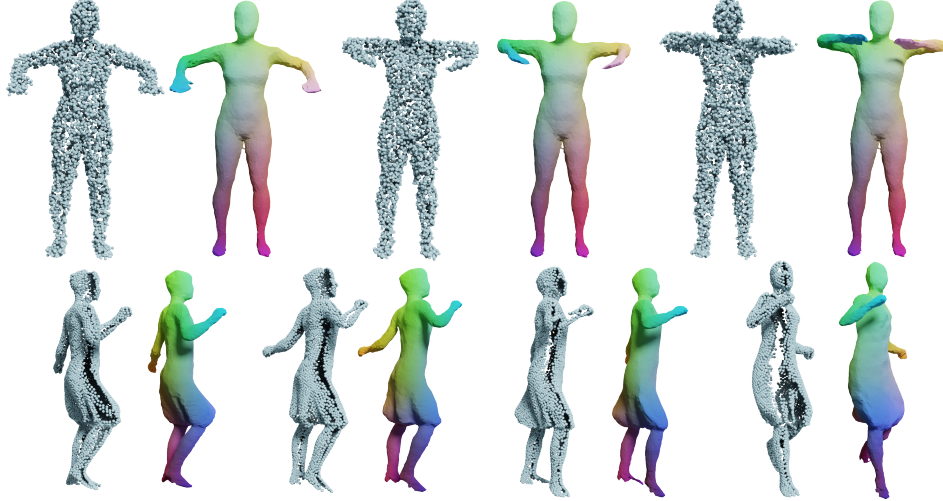


Figure 7: Results by our method on noisy data (top) and partially missing data (bottom).

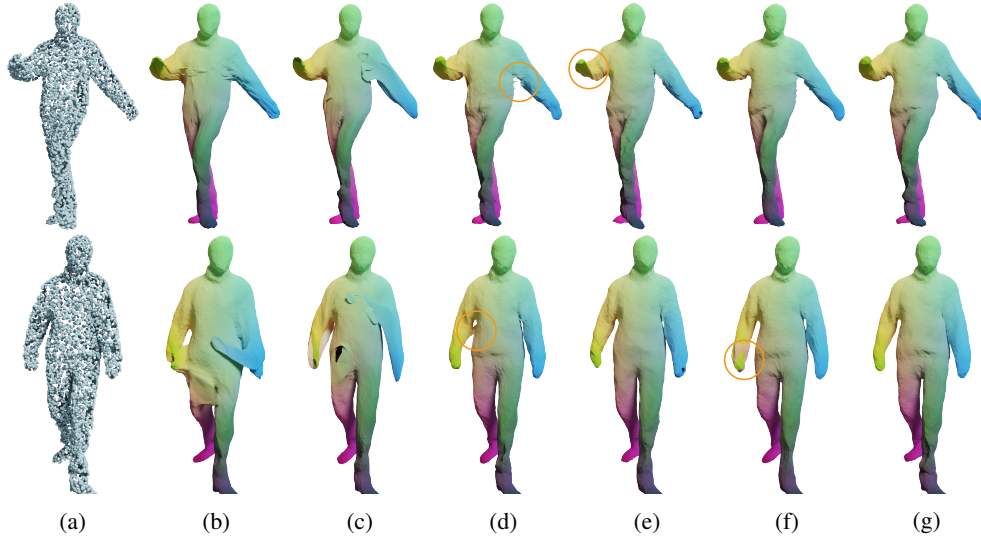


Figure 8: Comparison of visual results by different variants of the deformation field in our method. (a) Input; (b) Point-wise deformation based on an MLP; (c) Fixed blending weight formula; (d) Fixed control point positions; (e)  $|\mathbf{U}| = 10$ ; (f)  $|\mathbf{U}| = 100$ ; (g) Ours.

- *Pointwise deformation based on an MLP:* For any point  $\bar{\mathbf{v}} \in \mathbb{R}^3$  in the template surface and frame index  $k$ , we established a deformation function  $F_{\Psi}(\Gamma([\bar{\mathbf{v}}|k]))$  and obtained the deformed position  $\mathbf{v}^k = \bar{\mathbf{v}} + F_{\Psi}(\Gamma([\bar{\mathbf{v}}|k]))$ . Here,  $F_{\Psi}(\cdot)$  is an MLP with 5 linear layers and a feature dimension of 128.
- *Fixed blending weight formula:* We replaced the learnable blending weights in Eq. (6) by setting it to the value computed by  $\tilde{\omega}(\bar{\mathbf{v}}, \mathbf{u}_r)$  in Eq. (8) throughout the learning process.
- *Fixed control point positions:* We maintained the positions  $\mathbf{u}_r$  of the control points at their initial values.

From Tab. 3 and Fig. 8, the three variants produce worse quantitative and visual results than Ours, verifying the advantage of our proposed deformation field. Fig. 9 also visualizes the learned weights via Eq. (7) and those computed via Eq. (8) for blending, where we can see that the learned weights can capture the motion information and well handle the deformations for the parts with close spatial locations but inconsistent motions.

Table 3: Ablation studies of our method on the AMA dataset [52]. The best and second best results are highlighted in **bold** and underlined.

Variants	CD( $\times 10^{-4}$ ) $\downarrow$	NC $\uparrow$	F-0.5% $\uparrow$	F-1% $\uparrow$	Corr. ( $\times 10^{-2}$ ) $\downarrow$
MLP-Deform	0.412	0.909	0.917	0.618	5.91
w. $\tilde{\omega}(\bar{\mathbf{v}}, \mathbf{u}_r)$	0.475	0.911	0.890	0.564	3.26
Fixed $\{\mathbf{u}_r\}$	0.372	0.911	0.927	0.637	3.23
w.o. $L_{R-SDF}$	0.330	0.918	0.937	0.649	3.14
w.o. $L_{Norm}$	0.656	0.900	0.884	0.582	3.30
w.o. $L_{Smo}$	0.378	0.914	0.923	0.616	3.30
w.o. $L_{Shape}$	0.335	0.919	0.936	0.636	<u>2.91</u>
$ \mathbf{U}  = 10$	0.437	0.910	0.910	0.594	3.30
$ \mathbf{U}  = 30$ ( <b>Ours</b> )	<u>0.324</u>	<u>0.919</u>	<u>0.939</u>	<u>0.649</u>	<b>2.89</b>
$ \mathbf{U}  = 100$	<b>0.315</b>	<b>0.919</b>	<b>0.943</b>	<b>0.651</b>	3.16

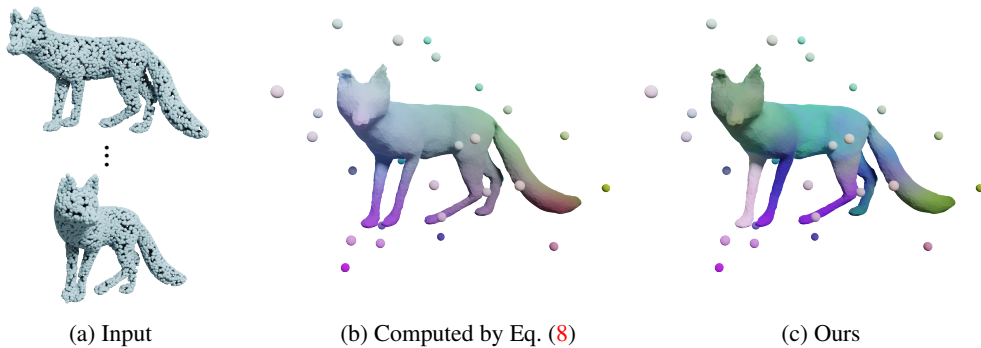


Figure 9: Visual learnable control points and blending weights. We assigned a color  $\mathbf{c}_r$  to each control point  $\mathbf{u}_r$  based on its spatial position, and obtained the color for each  $\bar{\mathbf{v}}$  by  $\sum_{r=1}^{|\mathbf{U}|} \omega(\bar{\mathbf{v}}, \mathbf{u}_r) \cdot \mathbf{c}_r$ . Closer colors indicate more similar deformation fields.

**2) Size of  $|\mathbf{U}|$ .** From Tab. 3 and Fig. 8, where we set different numbers of control points i.e., 10, 30, and 100, we can observe that too few control points result in insufficient degrees of freedom and suboptimal alignment, while too many control points can weaken local consistency. We set  $|\mathbf{U}| = 30$  as a balanced trade-off.

**3) Loss functions during temporal reconstruction.** To assess the effectiveness of various loss terms used in the temporal reconstruction stage, we individually excluded the robust SDF loss  $L_{R-SDF}$ , deformation smooth loss  $L_{Smo}$ , and shape maintenance loss  $L_{Shape}$ , while keeping other aspects unchanged. The results presented in Tab. 3 demonstrate their necessity and contributions.

**4) Keyframe selection and template surface learning.** Compared to directly setting the middle frame as a keyframe, Fig. 10 shows that the selected keyframe by our strategy is closer to the average shape. After learning the template surface, we also show the results of only using the fine stage (Fig. 10 (b)) and using the coarse-to-fine stage (Fig. 10 (c)). Based on Fig. 10 (c), we further show the enhanced template surface after the temporal reconstruction process.

## 5 Conclusion and Discussion

We introduced a new unsupervised temporally-consistent dynamic surface reconstruction framework for time-varying point cloud sequences. Technically, we integrated template surface representation based on the deformable tetrahedron and a learnable deformation field. We first proposed a coarse-to-fine learning strategy for constructing the template surface. Then we designed a learnable deformation field using the learnable control points and blending weights for temporally reconstruction. We jointly optimized the enhanced template surface and the learnable deformation field. Exper-

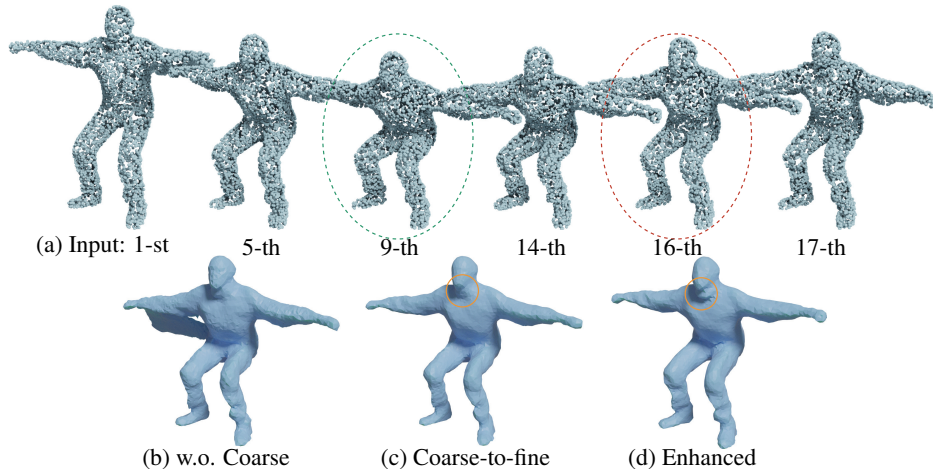


Figure 10: Visual results of the template surface learned from different settings. For input point clouds, we use the green circle to mark the middle frame and the red circle to mark the template frame we selected.

iments demonstrate that our proposed method performs even much better than SOTA supervised learning methods.

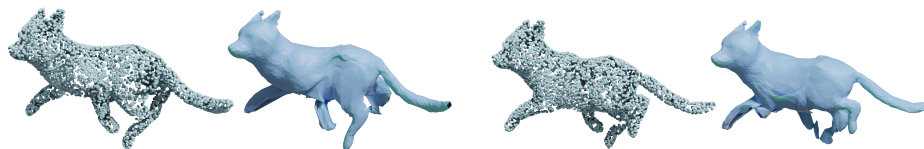


Figure 11: Failure case of our method.

Although our method has achieved good performance on many examples, it may encounter limitations in cases where the point cloud in certain areas is sparse or the local structure is elongated but exhibits significant non-rigid deformations (as depicted in the Fig. 11). This is attributed to our utilization of Chamfer distance as the alignment supervision, which restricts the establishment of correspondences between adjacent frames solely based on spatial proximity. Incorporating more robust metrics for shape alignment would enhance the effectiveness of our approach.

## References

- [1] Matan Atzmon and Yaron Lipman. Sal: Sign agnostic learning of shapes from raw data. In *IEEE Conf. Comput. Vis. Pattern Recog.*, pages 2565–2574, 2020.
- [2] C Bradford Barber, David P Dobkin, and Hannu Huhdanpaa. The quickhull algorithm for convex hulls. *ACM Transactions on Mathematical Software (TOMS)*, 22(4):469–483, 1996.
- [3] Federica Bogo, Javier Romero, Gerard Pons-Moll, and Michael J Black. Dynamic faust: Registering human bodies in motion. In *IEEE Conf. Comput. Vis. Pattern Recog.*, pages 6233–6242, 2017.
- [4] Alexandre Boulch and Renaud Marlet. Poco: Point convolution for surface reconstruction. In *IEEE Conf. Comput. Vis. Pattern Recog.*, pages 6302–6314, 2022.
- [5] Aljaz Bozic, Pablo Palafox, Michael Zollhofer, Justus Thies, Angela Dai, and Matthias Nießner. Neural deformation graphs for globally-consistent non-rigid reconstruction. In *IEEE Conf. Comput. Vis. Pattern Recog.*, pages 1450–1459, 2021.
- [6] Ricky TQ Chen, Yulia Rubanova, Jesse Bettencourt, and David K Duvenaud. Neural ordinary differential equations. *Adv. Neural Inform. Process. Syst.*, 31, 2018.

- [7] Cheng Chi and Shuran Song. Garmentnets: Category-level pose estimation for garments via canonical space shape completion. In *Int. Conf. Comput. Vis.*, pages 3324–3333, 2021.
- [8] Ranjana Roy Chowdhury and Deepti R Bathula. Ipnnet: Influential prototypical networks for few shot learning. *arXiv preprint arXiv:2208.09345*, 2022.
- [9] Mingsong Dou, Sameh Khamis, Yury Degtyarev, Philip Davidson, Sean Ryan Fanello, Adarsh Kowdle, Sergio Orts Escolano, Christoph Rhemann, David Kim, Jonathan Taylor, et al. Fusion4d: Real-time performance capture of challenging scenes. *ACM Trans. Graph.*, 35(4):1–13, 2016.
- [10] Yuval Eldar, Michael Lindenbaum, Moshe Porat, and Yehoshua Y Zeevi. The farthest point strategy for progressive image sampling. *IEEE Trans. Image Process.*, 6(9):1305–1315, 1997.
- [11] Wanquan Feng, Juyong Zhang, Hongrui Cai, Haofei Xu, Junhui Hou, and Hujun Bao. Recurrent multi-view alignment network for unsupervised surface registration. In *IEEE Conf. Comput. Vis. Pattern Recog.*, pages 10297–10307, 2021.
- [12] Yutong Feng, Yifan Feng, Haoxuan You, Xibin Zhao, and Yue Gao. Meshnet: Mesh neural network for 3d shape representation. In *Proceedings of the AAAI conference on artificial intelligence*, pages 8279–8286, 2019.
- [13] Rana Hanocka, Amir Hertz, Noa Fish, Raja Giryes, Shachar Fleishman, and Daniel Cohen-Or. Meshcnn: a network with an edge. *ACM Trans. Graph.*, 38(4):1–12, 2019.
- [14] Jiahui Huang, Zan Gojcic, Matan Atzmon, Or Litany, Sanja Fidler, and Francis Williams. Neural kernel surface reconstruction. In *IEEE Conf. Comput. Vis. Pattern Recog.*, pages 4369–4379, 2023.
- [15] Boyan Jiang, Xinlin Ren, Mingsong Dou, Xiangyang Xue, Yanwei Fu, and Yinda Zhang. Lord: Local 4d implicit representation for high-fidelity dynamic human modeling. In *Eur. Conf. Comput. Vis.*, pages 307–326. Springer, 2022.
- [16] Boyan Jiang, Yinda Zhang, Xingkui Wei, Xiangyang Xue, and Yanwei Fu. H4d: human 4d modeling by learning neural compositional representation. In *IEEE Conf. Comput. Vis. Pattern Recog.*, pages 19355–19365, 2022.
- [17] Michael Kazhdan, Matthew Bolitho, and Hugues Hoppe. Poisson surface reconstruction. In *Proceedings of the fourth Eurographics symposium on Geometry processing*, volume 7, page 0, 2006.
- [18] Michael Kazhdan and Hugues Hoppe. Screened poisson surface reconstruction. *ACM Trans. Graph.*, 32(3):1–13, 2013.
- [19] Diederik P Kingma and Jimmy Ba. Adam: A method for stochastic optimization. *arXiv preprint arXiv:1412.6980*, 2014.
- [20] Ravikrishna Kolluri. Provably good moving least squares. *ACM Transactions on Algorithms (TALG)*, 4(2):1–25, 2008.
- [21] Jiahui Lei and Kostas Daniilidis. Cadex: Learning canonical deformation coordinate space for dynamic surface representation via neural homeomorphism. In *IEEE Conf. Comput. Vis. Pattern Recog.*, pages 6624–6634, 2022.
- [22] Hao Li, Bart Adams, Leonidas J Guibas, and Mark Pauly. Robust single-view geometry and motion reconstruction. *ACM Trans. Graph.*, 28(5):1–10, 2009.
- [23] Hao Li, Robert W. Sumner, and Mark Pauly. Global correspondence optimization for non-rigid registration of depth scans. *Comput. Graph. Forum*, 27(5):1421–1430, 2008.
- [24] Yang Li and Tatsuya Harada. Non-rigid point cloud registration with neural deformation pyramid. *Adv. Neural Inform. Process. Syst.*, 35:27757–27768, 2022.
- [25] Yang Li, Hikari Takehara, Takafumi Taketomi, Bo Zheng, and Matthias Nießner. 4dcomplete: Non-rigid motion estimation beyond the observable surface. In *Int. Conf. Comput. Vis.*, pages 12706–12716, 2021.
- [26] Yangyan Li, Rui Bu, Mingchao Sun, Wei Wu, Xinhan Di, and Baoquan Chen. Pointcnn: Convolution on x-transformed points. *Adv. Neural Inform. Process. Syst.*, 31, 2018.
- [27] Shi-Lin Liu, Hao-Xiang Guo, Hao Pan, Peng-Shuai Wang, Xin Tong, and Yang Liu. Deep implicit moving least-squares functions for 3d reconstruction. In *IEEE Conf. Comput. Vis. Pattern Recog.*, pages 1788–1797, 2021.

- [28] Xingyu Liu, Charles R Qi, and Leonidas J Guibas. Flownet3d: Learning scene flow in 3d point clouds. In *IEEE Conf. Comput. Vis. Pattern Recog.*, pages 529–537, 2019.
- [29] Matthew Loper, Naureen Mahmood, Javier Romero, Gerard Pons-Moll, and Michael J. Black. SMPL: a skinned multi-person linear model. *ACM Trans. Graph.*, 34(6):248:1–248:16, 2015.
- [30] William E Lorensen and Harvey E Cline. Marching cubes: A high resolution 3d surface construction algorithm. *ACM siggraph computer graphics*, 21(4):163–169, 1987.
- [31] Lars Mescheder, Michael Oechsle, Michael Niemeyer, Sebastian Nowozin, and Andreas Geiger. Occupancy networks: Learning 3d reconstruction in function space. In *IEEE Conf. Comput. Vis. Pattern Recog.*, pages 4460–4470, 2019.
- [32] Richard A Newcombe, Dieter Fox, and Steven M Seitz. Dynamicfusion: Reconstruction and tracking of non-rigid scenes in real-time. In *IEEE Conf. Comput. Vis. Pattern Recog.*, pages 343–352, 2015.
- [33] Gregory M Nielson. Dual marching tetrahedra: Contouring in the tetrahedral environment. In *International Symposium on Visual Computing*, pages 183–194. Springer, 2008.
- [34] Michael Niemeyer, Lars Mescheder, Michael Oechsle, and Andreas Geiger. Occupancy flow: 4d reconstruction by learning particle dynamics. In *Int. Conf. Comput. Vis.*, pages 5379–5389, 2019.
- [35] Pablo Palafox, Aljaž Božič, Justus Thies, Matthias Nießner, and Angela Dai. Npms: Neural parametric models for 3d deformable shapes. In *Int. Conf. Comput. Vis.*, pages 12695–12705, 2021.
- [36] Jeong Joon Park, Peter Florence, Julian Straub, Richard Newcombe, and Steven Lovegrove. DeepSDF: Learning continuous signed distance functions for shape representation. In *IEEE Conf. Comput. Vis. Pattern Recog.*, pages 165–174, 2019.
- [37] Keunhong Park, Utkarsh Sinha, Jonathan T Barron, Sofien Bouaziz, Dan B Goldman, Steven M Seitz, and Ricardo Martin-Brualla. Nerfies: Deformable neural radiance fields. In *Int. Conf. Comput. Vis.*, pages 5865–5874, 2021.
- [38] Songyou Peng, Chiyu Jiang, Yiyi Liao, Michael Niemeyer, Marc Pollefeys, and Andreas Geiger. Shape as points: A differentiable poisson solver. *Adv. Neural Inform. Process. Syst.*, 34:13032–13044, 2021.
- [39] Songyou Peng, Michael Niemeyer, Lars Mescheder, Marc Pollefeys, and Andreas Geiger. Convolutional occupancy networks. In *Eur. Conf. Comput. Vis.*, pages 523–540. Springer, 2020.
- [40] Charles R Qi, Hao Su, Kaichun Mo, and Leonidas J Guibas. Pointnet: Deep learning on point sets for 3d classification and segmentation. In *IEEE Conf. Comput. Vis. Pattern Recog.*, pages 652–660, 2017.
- [41] Charles Ruizhongtai Qi, Li Yi, Hao Su, and Leonidas J Guibas. Pointnet++: Deep hierarchical feature learning on point sets in a metric space. *Adv. Neural Inform. Process. Syst.*, 30, 2017.
- [42] Nasim Rahaman, Aristide Baratin, Devansh Arpit, Felix Draxler, Min Lin, Fred Hamprecht, Yoshua Bengio, and Aaron Courville. On the spectral bias of neural networks. In *International Conference on Machine Learning*, pages 5301–5310. PMLR, 2019.
- [43] Davis Rempe, Tolga Birdal, Yongheng Zhao, Zan Gojcic, Srinath Sridhar, and Leonidas J Guibas. Caspr: Learning canonical spatiotemporal point cloud representations. *Adv. Neural Inform. Process. Syst.*, 33:13688–13701, 2020.
- [44] Siyu Ren, Junhui Hou, Xiaodong Chen, Ying He, and Wenping Wang. Geoudf: Surface reconstruction from 3d point clouds via geometry-guided distance representation. In *Int. Conf. Comput. Vis.*, pages 14214–14224, 2023.
- [45] Tianchang Shen, Jun Gao, Kangxue Yin, Ming-Yu Liu, and Sanja Fidler. Deep marching tetrahedra: a hybrid representation for high-resolution 3d shape synthesis. *Adv. Neural Inform. Process. Syst.*, 34:6087–6101, 2021.
- [46] Tianchang Shen, Jacob Munkberg, Jon Hasselgren, Kangxue Yin, Zian Wang, Wenzheng Chen, Zan Gojcic, Sanja Fidler, Nicholas Sharp, and Jun Gao. Flexible isosurface extraction for gradient-based mesh optimization. *ACM Trans. Graph.*, 42(4):1–16, 2023.

- [47] Soshi Shimada, Vladislav Golyanik, Edgar Tretschk, Didier Stricker, and Christian Theobalt. Dispvoxnets: Non-rigid point set alignment with supervised learning proxies. In *2019 international conference on 3D vision (3DV)*, pages 27–36. IEEE, 2019.
- [48] Miroslava Slavcheva, Maximilian Baust, Daniel Cremers, and Slobodan Ilic. Killingfusion: Non-rigid 3d reconstruction without correspondences. In *IEEE Conf. Comput. Vis. Pattern Recog.*, pages 1386–1395, 2017.
- [49] Robert W. Sumner, Johannes Schmid, and Mark Pauly. Embedded deformation for shape manipulation. *TOG*, 26(3):80:1–80:7, 2007.
- [50] Jiapeng Tang, Dan Xu, Kui Jia, and Lei Zhang. Learning parallel dense correspondence from spatio-temporal descriptors for efficient and robust 4d reconstruction. In *IEEE Conf. Comput. Vis. Pattern Recog.*, pages 6022–6031, 2021.
- [51] Edgar Tretschk, Ayush Tewari, Vladislav Golyanik, Michael Zollhöfer, Christoph Lassner, and Christian Theobalt. Non-rigid neural radiance fields: Reconstruction and novel view synthesis of a dynamic scene from monocular video. In *Int. Conf. Comput. Vis.*, pages 12959–12970, 2021.
- [52] Daniel Vlasic, Ilya Baran, Wojciech Matusik, and Jovan Popović. Articulated mesh animation from multi-view silhouettes. *ACM Trans. Graph.*, 27(3):97:1–97:9, August 2008.
- [53] Zhenchao Wu, Kun Li, Yu-Kun Lai, and Jingyu Yang. Global as-conformal-as-possible non-rigid registration of multi-view scans. In *2019 IEEE International Conference on Multimedia and Expo (ICME)*, pages 308–313. IEEE, 2019.
- [54] Jingyu Yang, Daoliang Guo, Kun Li, Zhenchao Wu, and Yu-Kun Lai. Global 3d non-rigid registration of deformable objects using a single rgb-d camera. *IEEE Trans. Image Process.*, 28(10):4746–4761, 2019.
- [55] Yuxin Yao, Bailin Deng, Weiwei Xu, and Juyong Zhang. Quasi-newton solver for robust non-rigid registration. In *IEEE Conf. Comput. Vis. Pattern Recog.*, pages 7600–7609, 2020.
- [56] Yuxin Yao, Bailin Deng, Weiwei Xu, and Juyong Zhang. Fast and robust non-rigid registration using accelerated majorization-minimization. *IEEE Trans. Pattern Anal. Mach. Intell.*, 2023.
- [57] Tarun Yenamandra, Ayush Tewari, Florian Bernard, Hans-Peter Seidel, Mohamed Elgharib, Daniel Cremers, and Christian Theobalt. i3dmm: Deep implicit 3d morphable model of human heads. In *IEEE Conf. Comput. Vis. Pattern Recog.*, pages 12803–12813, 2021.
- [58] Andy Zeng, Shuran Song, Matthias Nießner, Matthew Fisher, Jianxiong Xiao, and Thomas Funkhouser. 3dmatch: Learning local geometric descriptors from rgb-d reconstructions. In *IEEE Conf. Comput. Vis. Pattern Recog.*, pages 1802–1811, 2017.
- [59] Yiming Zeng, Yue Qian, Zhiyu Zhu, Junhui Hou, Hui Yuan, and Ying He. Corrnnet3d: Un-supervised end-to-end learning of dense correspondence for 3d point clouds. In *IEEE Conf. Comput. Vis. Pattern Recog.*, pages 6052–6061, 2021.
- [60] Baowen Zhang, Jiahe Li, Xiaoming Deng, Yinda Zhang, Cuixia Ma, and Hongan Wang. Self-supervised learning of implicit shape representation with dense correspondence for deformable objects. In *Int. Conf. Comput. Vis.*, pages 14268–14278, 2023.
- [61] Silvia Zuffi, Angjoo Kanazawa, David W Jacobs, and Michael J Black. 3d menagerie: Modeling the 3d shape and pose of animals. In *IEEE Conf. Comput. Vis. Pattern Recog.*, pages 6365–6373, 2017.

## Supplementary Material

### More visual results

We present more visual results in this section and showcase the complete action sequences in the supplementary video.

**Comparisons with state-of-the-art methods.** We present additional visual results for comparisons with LPDC [50] and Cadex [21] on the DFAUST dataset [3] (Fig. 12), AMA dataset [52] (Fig. 13) and DT4D dataset [25] (Fig. 15). It is evident that our method outperforms other approaches.



Figure 12: Comparison of visual results by different methods on the DFAUST dataset.

**Ablation study.** Additionally, Fig. 14 illustrates the visual results of our method when different loss terms are omitted. We can see that our method, incorporating all loss terms, achieves the best results.

**Performance of our method on noisy data and partially missing data.** Furthermore, in Fig. 16, we showcase more visual results of our method applied to noisy data constructed from the DFAUST dataset [3] and partially missing data constructed from AMA dataset [52], respectively.



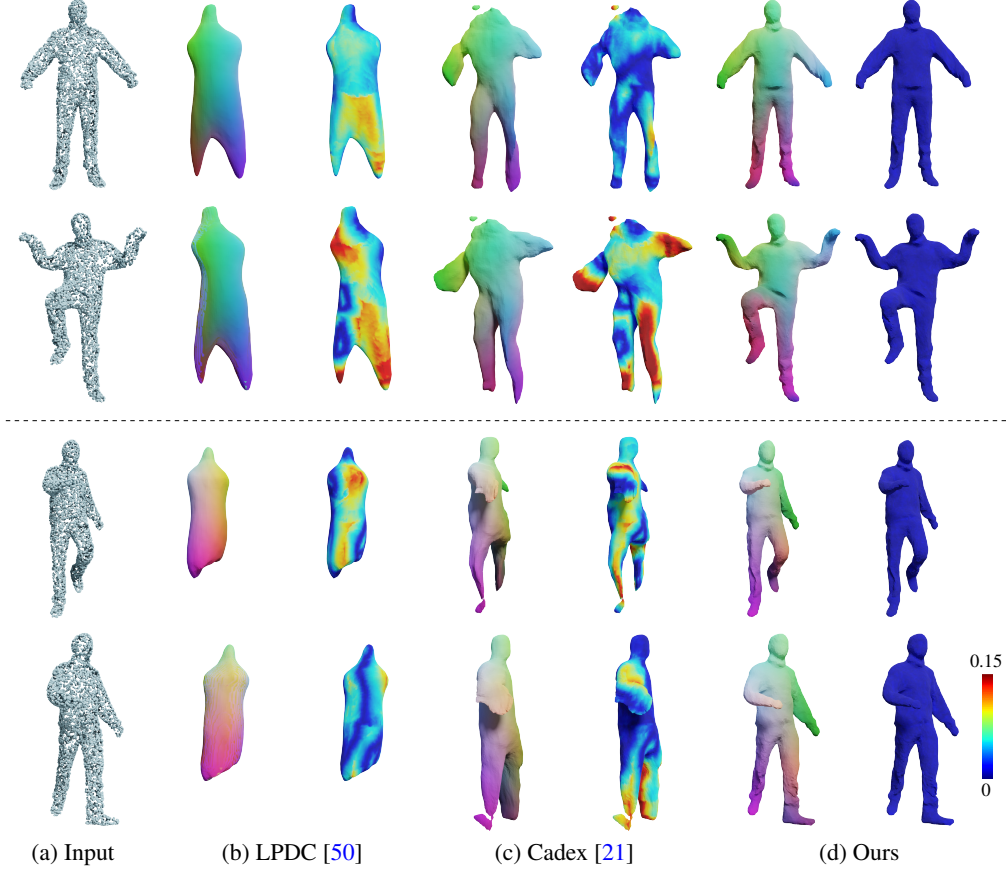


Figure 13: Comparison of visual results by different methods on the AMA dataset [52].

### Technical Details

In this section, we explain the definitions for some loss functions and evaluation metrics mentioned in the paper. The Chamfer Distance between  $\mathbf{X}$  and  $\mathbf{Y}$  is defined as

$$CD_{\ell_p}(\mathbf{X}, \mathbf{Y}) = \frac{1}{|\tilde{\mathbf{X}}|} \sum_{\mathbf{x} \in \tilde{\mathbf{X}}} \|\mathbf{x} - \hat{\mathbf{y}}\|_{\ell_p} + \frac{1}{|\tilde{\mathbf{Y}}|} \sum_{\mathbf{y} \in \tilde{\mathbf{Y}}} \|\mathbf{y} - \hat{\mathbf{x}}\|_{\ell_p}, \quad (15)$$

where  $p = 1, 2$ .  $\hat{\mathbf{y}} \in \tilde{\mathbf{Y}}$  and  $\hat{\mathbf{x}} \in \tilde{\mathbf{X}}$  are the closest points for the  $\mathbf{x}$  and  $\mathbf{y}$  respectively. When  $\mathbf{X}(\mathbf{Y})$  is a point set,  $\tilde{\mathbf{X}} = \mathbf{X}(\tilde{\mathbf{Y}} = \mathbf{Y})$ . When  $\mathbf{X}(\mathbf{Y})$  represents a mesh,  $\tilde{\mathbf{X}}(\tilde{\mathbf{Y}})$  denotes the sampling point on the mesh. In the learning phase, we set the number of sampling points to  $10^4$ , and during the evaluation, we set the number of sampling points to  $10^5$ .

In Eqs. (3) and (10), the normal consistency of  $\mathbf{X}$  and  $\mathbf{Y}$  is defined as

$$NC_{\ell_1}(\mathbf{X}, \mathbf{Y}) = \frac{1}{|\mathbf{N}_x|} \sum_{\mathbf{n}_x \in \mathbf{N}_x} |1 - |\langle \mathbf{n}_x, \mathbf{n}_{\hat{\mathbf{y}}} \rangle|| + \frac{1}{|\mathbf{N}_y|} \sum_{\mathbf{n}_y \in \mathbf{N}_y} |1 - |\langle \mathbf{n}_y, \mathbf{n}_{\hat{\mathbf{x}}} \rangle||, \quad (16)$$

where  $\mathbf{N}_x$  and  $\mathbf{N}_y$  are the normal sets of  $\tilde{\mathbf{X}}$  and  $\tilde{\mathbf{Y}}$  respectively,  $\mathbf{n}_{\hat{\mathbf{y}}} \in \mathbf{N}_y$  and  $\mathbf{n}_{\hat{\mathbf{x}}} \in \mathbf{N}_x$  are the corresponding normals of  $\hat{\mathbf{y}}$  and  $\hat{\mathbf{x}}$  respectively.  $\langle \cdot, \cdot \rangle$  is the inner product.

Following [31, 38, 44], the F-score to evaluate the reconstruction accuracy is defined as:

$$\text{F-score}(\mathbb{M}_k, \mathbb{M}_k^{\text{GT}}, \epsilon) = \frac{2 \cdot \text{Recall} \cdot \text{Precision}}{\text{Recall} + \text{Precision}}, \quad (17)$$

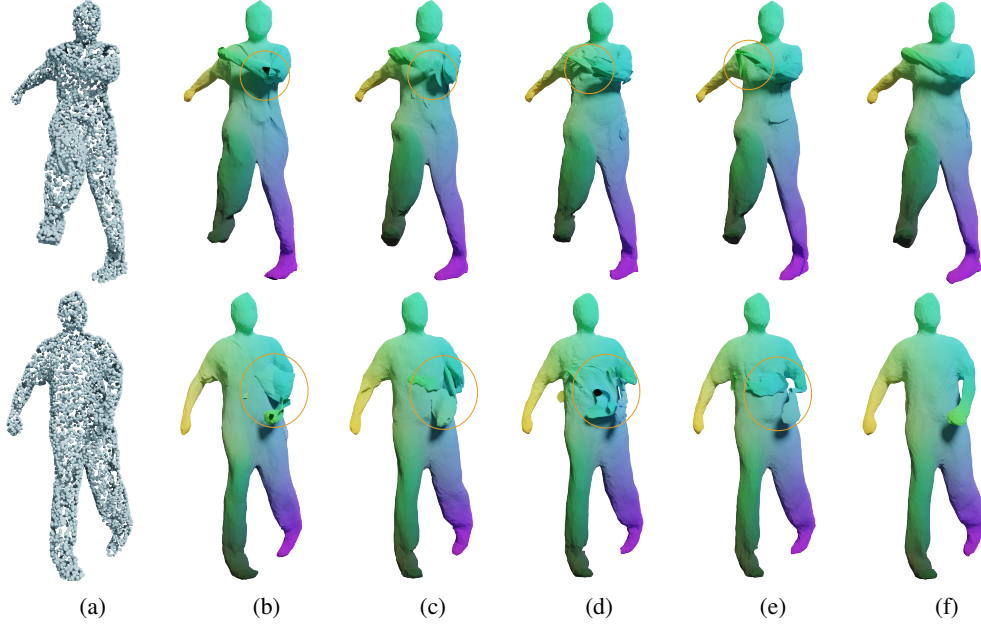


Figure 14: Comparison of visual results by different variants of excluding a certain loss in our method. (a) Input; (b) w.o.  $L_{R-SDF}$ ; (c) w.o.  $L_{Norm}$ ; (d) w.o.  $L_{Smo}$ ; (e) w.o.  $L_{Shape}$ ; (f) Ours.

where

$$\text{Recall}(\mathbb{M}_k, \mathbb{M}_k^{\text{GT}}, \epsilon) = \left| \left\{ \mathbf{v}_1 \in \tilde{\mathbf{V}}_k, \text{s.t. } \min_{\mathbf{v}_2 \in \tilde{\mathbf{V}}_k^{\text{GT}}} \|\mathbf{v}_1 - \mathbf{v}_2\| < \epsilon \right\} \right|,$$

$$\text{Precision}(\mathbb{M}_k, \mathbb{M}_k^{\text{GT}}, \epsilon) = \left| \left\{ \mathbf{v}_2 \in \tilde{\mathbf{V}}_k^{\text{GT}}, \text{s.t. } \min_{\mathbf{v}_1 \in \tilde{\mathbf{V}}_k} \|\mathbf{v}_1 - \mathbf{v}_2\| < \epsilon \right\} \right|.$$

Here  $\mathbb{M}_k^{\text{GT}}$  is the  $k$ -th ground-truth mesh,  $\tilde{\mathbf{V}}_k(\tilde{\mathbf{V}}_k^{\text{GT}})$  is the point set of the randomly sampling  $10^5$  points from  $\mathbb{M}_k(\mathbb{M}_k^{\text{GT}})$ . We set  $\epsilon$  to 0.5% or 1%, and compute mean value of  $\text{F-score}(\mathbb{M}_k, \mathbb{M}_k^{\text{GT}}, \epsilon)$  ( $k = 1, 2, \dots, K$ ) to get F-0.5% or F-1%.

We denote  $\{\mathbf{V}^{\text{GT}}(k)\}_k$  as the temporally consistent corresponding points on the ground-truth surfaces. We set  $|\mathbf{V}^{\text{GT}}(k)| = 10^5$ . In the first frame, we construct the index set of nearest points:

$$\text{Index} = \{\rho_i | \mathbf{v}_{\rho_i} = \arg \min_{\mathbf{v} \in \mathbf{V}_1} \|\mathbf{v} - \mathbf{v}_i^{\text{GT}}(1)\|\},$$

where  $\mathbf{V}_1$  is the vertex set of 1-st reconstructed mesh  $\mathbb{M}_1$ ,  $\mathbf{v}_i^{\text{GT}}(1) \in \mathbf{V}^{\text{GT}}(1)$ . Following [34, 21], the Correspondences Error is defined as

$$\text{Corr.} = \frac{1}{|\text{Index}| \cdot K} \sum_{k=1}^K \sum_{\rho_i \in \text{Index}} \|\mathbf{v}_{\rho_i}^k - \mathbf{v}_i^{\text{GT}}(k)\|.$$

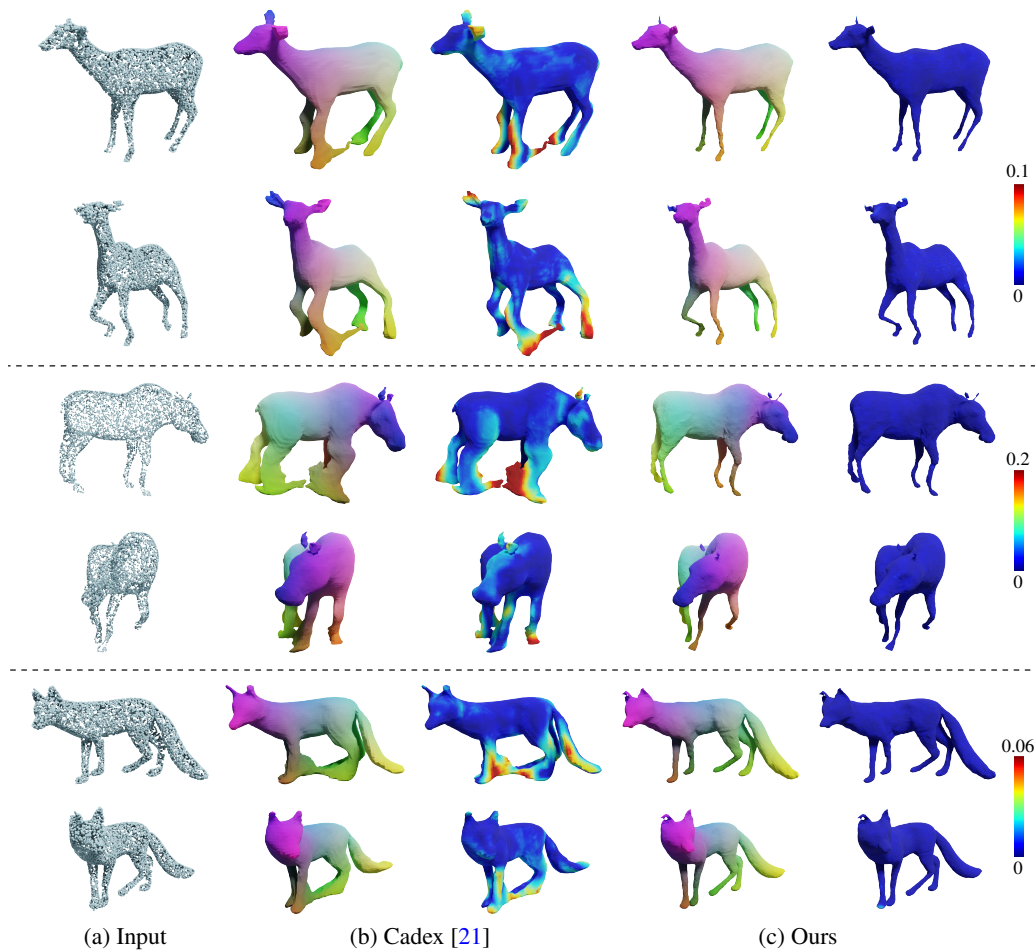


Figure 15: Comparison of visual results by different methods on the DT4D dataset.

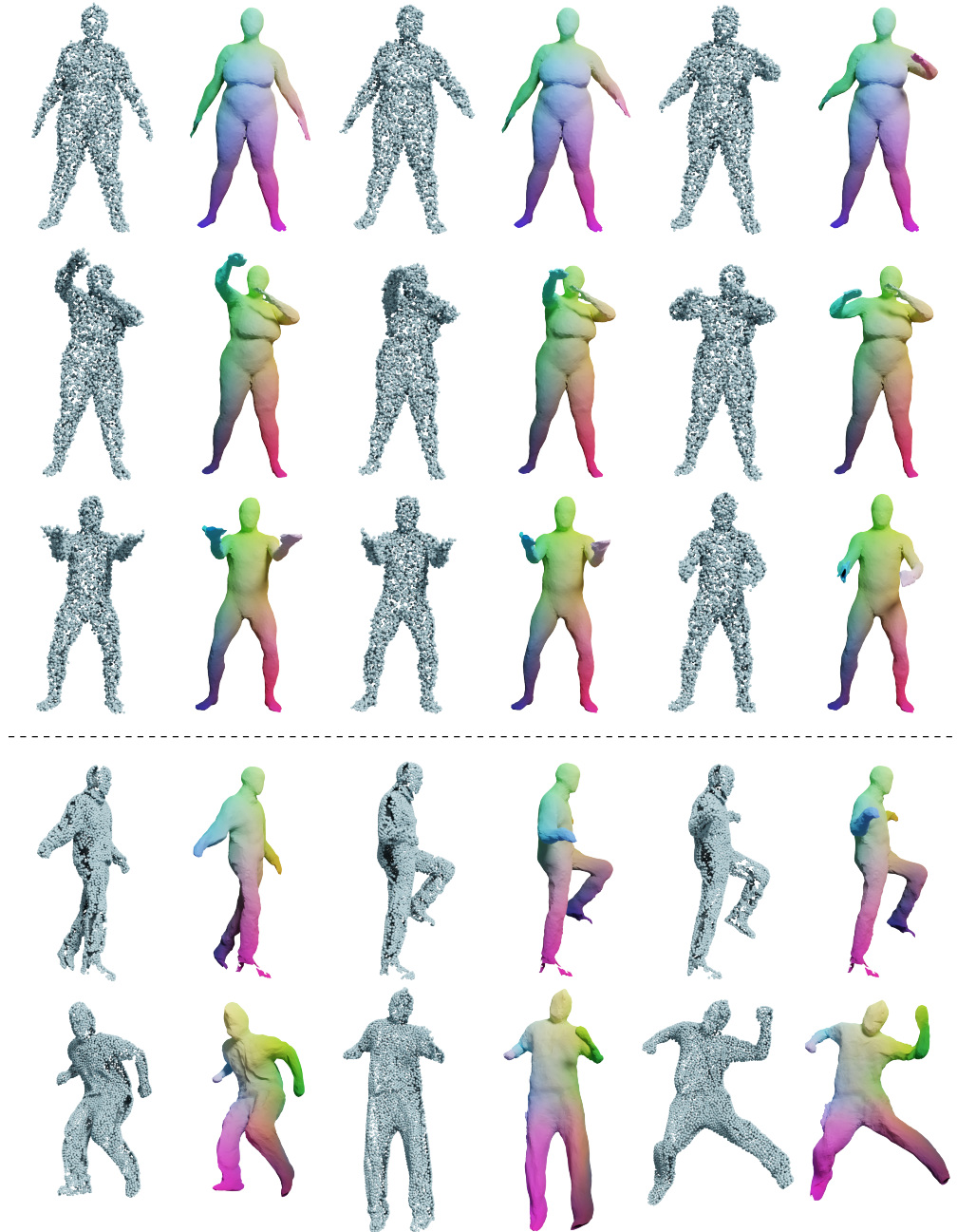


Figure 16: Visual results of our method on constructed noisy data from the DFAUST dataset [3] (Top) and partially missing data from AMA dataset [52] (Bottom).